# Supplementary Information to Adhesion Dynamics of Functionalized Nanocarriers to Endothelial Cells: A Dissipative Particles Dynamics Study

## Contents

### Simulation technique: Dissipative Particles Dynamics:

As a particle-based simulation approach, DPD was constructed to discover correct hydrodynamic behavior in fluids[1]. For each particle at each time and position ($r_i$), the velocity ($v_i$) equation of motion is solved, and forces are determined and updated at each time step. It contains conservative ($\mathbf{F^C}$), dissipative ($\mathbf{F^D}$), and random force ($\mathbf{F^R}$) as pairwise interparticle forces. Employing these forces creates each DPD particle as a frictional noisy soft sphere that interacts with other DPD spheres over time. The total force within the cut-off distance which is used by $j^{th}$ neighboring particle on the $i^{th}$ particle is:

$$F_i = \sum_{j \neq i} F_{i,j}^C + F_{i,j}^D + F_{i,j}^R \qquad (1)$$

The conservative force $\mathbf{F^C}$ is a soft potential that reduces linearly with respect to the center-to-center distance of two particles (eq. 2). By selecting a proper repulsion coefficient between particle i and j ($a_{ij}$), this force can achieve equilibrium thermodynamic properties like compressibility[2]. The dissipative force $\mathbf{F^D}$ (eq. 3) displays the viscous resistance of fluids, and its value is associated with the velocity of the two particles working between center to center of particles and expects to decrease relative velocities and kinetic energy of DPD particles. The Brownian motion in the system is characterized by random force $\mathbf{F^R}$ (eq. 4), which with the help of $\mathbf{F^D}$, regulates the temperature of the system. A proper correlation among the values of these forces ($\delta_{ij}$, $\gamma_{ij}$) and the weight function is necessary to maintain a constant temperature. The fluctuation-dissipation theorem (eq. 5) unites these forces and offers a relationship between the temperature of the system and the values of these forces.

$$F_{i,j}^C = a_{ij} W_{ij}^C(r_{ij}) e_{ij}, \qquad (2)$$

$$F_{i,j}^D = -\gamma_{ij} W_{ij}^D(r_{ij})(v_{ij}.e_{ij})e_{ij}, \qquad (3)$$

$$F_{i,j}^R = \delta_{ij} W_{ij}^R(r_{ij})\frac{\theta_{ij}}{\sqrt{\Delta t}}e_{ij}, \qquad (4)$$

$$\frac{\delta_{ij}^2}{2\gamma_{ij}} = k_B T,$$

$$W_{ij}^D(r_{ij}) = (W_{ij}^R(r_{ij}))_2, \qquad (5)$$

$r_{ij} = r_i - r_j$, is the vector distance between the particles, $r_{ij} = |r_{ij}|$ and the unit vector $e_{ij}$ is given by $e_{ij} = \dfrac{r_{ij}}{r_{ij}}$. The relative velocity of the pair of particles i and j is $v_{ij} = v_i - v_j$, and $\theta_{ij}$ represent a randomly fluctuating variable with Gaussian statistics.

At distances smaller than the cut-off radius conservative, dissipative and random weight functions are $W_{ij}^C(r_{ij}), W_{ij}^D(r_{ij})$, and $W_{ij}^R(r_{ij})$ respectively. These weight functions have the structure: $W_{ij}^C(r_{ij}) = 1 - |r_{ij}|/r_c$, $W_{ij}^D(|r_{ij}|) = W_{ij}^R(r_{ij})^2 = (1 - r_{ij}/r_c)^2$ at $r_{ij} < r_c$, and 0 for any $r_{ij} > r_c$. The fluctuation-dissipation theorem relates the dissipative and random weight functions which guarantees that the momentum is conserved and the hydrodynamic is preserved.

According to the original paper of Groot and Warren[3], the water-water repulsion $a_{ss}$ parameter is fixed relating to the adimensional compressibility of water $k_T^{-1}$. Comparing the equation of state of a DPD simulation and an experiment of water at room temperature results in $a_{ss} = 25\, k_B T/Rc$.

In this study, the length scales are chosen based on the macroscopic properties of the EG layer in the water.[4] The physical length scale $l_{phys}$ =12.5 nm is calculated according to the experimentally obtained distance of anchor points of the glycocalyx chains $d_{phys}$ =20 nm and the space between anchor points of EG chains in our simulation. This choice of the physical units in our DPD simulation provides the EG thickness in the range of thickness for the actual EG layer (100nm to 1000nm )[5], therefore, validating our choice of repulsion parameters and model against experimental observations.

To manage the distribution of ligands on the NCs surface, initially, we calculate the number of ligands for each ligand density and randomly distribute these ligands on the outer layer of the NC. We tether the one end of ligand chains on those randomly selected, but distinct surface beads of the outer layer of each NC. For instance, in the case of an 8rc disc with 152 ligands, we identify 152 random beads on the disc's surface area and attach the ligands to them. We have three ligand

densities: bare, low and high ligand density. The low ligand density is 0.375 nm$^{-2}$ and the high ligand density is 0.75 nm$^{-2}$ (typical of biomedical application).

As mentioned earlier, we maintain a constant surface area for different shapes. Consequently, at identical ligand densities, all shapes have the same number of ligands. For instance, for 8rc rod, disc, and sphere, each with equal surface areas, we utilize 76 ligands to achieve a ligand density of 0.375 nm$^{-2}$ and 152 ligands to attain a ligand density of 0.75 nm$^{-2}$. Therefore there is not any potential variations in ligand distribution between different NC shapes. For NCs with various sizes there are different surface areas. To maintain a consistent ligand density, we tether an appropriate number of ligands. For example, at a ligand density of 0.75 nm$^{-2}$, we use 152 ligands for 8rc, 340 ligands for 12rc, and 604 ligands for 16rc shapes of NCs.

The adhesion of functionalized NCs to endothelial cells with details such as NC, ligands, EG layer, receptors, water, and substrate have been studied through continuum modelings[4,6]. However, investigating NCs adhesion to the endothelial cell with all the details above using DPD simulation is a significant improvement on the state-of-the-art.

It should be noted that the DPD thermostat is compatible with hydrodynamics on large scales and is hence useful to investigate the dynamics even under a thermal non-equilibrium state[7].

In fact, the potential energy of our samples represents the sum of all non-bonded interactions between NC's shell and ligands, with EG layer, water, receptors, and wall beads. These mainly attractive interactions act as driving forces for the diffusion of NC into the EG layer. Average energies are stored at each time step. The potential energy of the system is determined as an integral of conservative forces and is shown in the equation 6.

$$PE = \int \left(a_{ij}\left(1 - \frac{r_{ij}}{r_c}\right)r_{ij}\right)dr_{ij} \tag{6}$$

The time evolution of conservative energy of a system in a DPD simulation was investigated by Wang et.al[8] and indicated that due to the presence of the random and dissipative forces (i.e., a thermostat) in DPD simulations, the system always maintains the thermal equilibrium.

Generally, the calculation of potential energy is straightforward however identifying the entropy is a complex task. To study the conformation of the EG layer, receptors, ligands and the shell of NCs, an expression that provides an approximate evaluation of the entropy is enough.

A conformational entropy is computed using the following equation 7.[9]

$$S_2 = -2\pi\rho k_B \int_0^\infty [g(r)lng(r) - g(r) + 1]r^2 dr, \tag{7}$$

Where $\rho$ is the density of the system, and the radial distribution function is g(r).

To identify local structures, $S_2$ could be used as a fingerprint if it properly applied to different atoms. The projection on atom i is obtained from the equation:

$$s_s^i = -2\pi\rho k_B \int_0^{r_m} \left[ g_m^i(r) \ln g_m^i(r) - g_m^i(r) + 1 \right] r^2 dr,$$

(8)

Where $g_m^i$ is the radial distribution function centered at the $i_{th}$ atom and $r_m$ is an upper integration limit. This entropy calculation method provides an instantaneous entropic snapshot of the system at each position within the simulation cell which can be investigated as a function of time. In other words this model can be used properly without prior knowledge of the physical state of the system therefore it can be applied for dynamic systems where every step is not equilibrated.[10–14]

According to Sefiddashti et al [10] the radial distribution function (RDF) in this method is not an ensemble-averaged over all atoms in the system rather it contains configurational information only within the immediate neighborhood of a particular atom and thus provides local entropy. On the other hand, our goal is not obtaining a precise absolute value for the entropy of the system rather is detecting a sharp change in configurational entropy which is produced by the NC penetration.

According to Piaggi et al.[9] this entropy fingerprint can distinguish ordered structures in a complex situation. In fact the g(r) is normalized by the local density around each atom. This is helpful when dealing with inhomogeneous system such as those that have surfaces (like the interface of EG/water and surface of NCs and ligands). Ghaffarizadeh et al.[15] shows that total entropy is calculated as a weighted average of the component entropies. This form of entropy decomposed by particle type and was used for soft materials.[11,12]

During the adsorption and penetration of NC to endothelial cells, entropy changes contain four main components:

(1) The change in entropy of EG chains due to changes in their conformation is called EG entropy.
(2) The change in entropy of the NC shell which is caused by the flexibility of the soft NCs shell and is called shell entropy.
(3) The change in entropy of ligands related to change in their conformation and is called ligand entropy
(4) The change in entropy of receptors associated with changes in their conformation is called receptor entropy

To quantify the size of the EG chains as a function of NCs penetration, their radius of gyration tensor in the Z axis (Rg_Z) in the water is computed. Rg_Z of EG chains is employed as a representative of their morphological properties. In order to compare Rg_Z plots of all different samples, only the $30*10^5$ time steps of the penetration stage are illustrated.

To investigate dynamics, for all the constructed NCs, the translational motion of the center of mass is explored. For calculating the translational motion of the NCs, the mean-square displacement (MSD) is determined (Equation 9).

$$MSD\ (\tau) = \langle (\vec{r}(t + \Delta t) - \vec{r}(t))^2 \rangle,$$

(9)

where $\Delta t$ is the interval time between the two positions. To examine the diffusion of the NC to the EG layer, mean-square displacement tensors in the Z axis (Z_MSD) and the X axis (X_MSD) of NCs are recorded.

I.    Effect of shape:

In figure S1 we investigate the shape effect on penetration of 12 $R_c$ bare NCs. The time evolution of Z_MSD, potential energy and shell entropy of the rod, sphere, and the disc are compared.
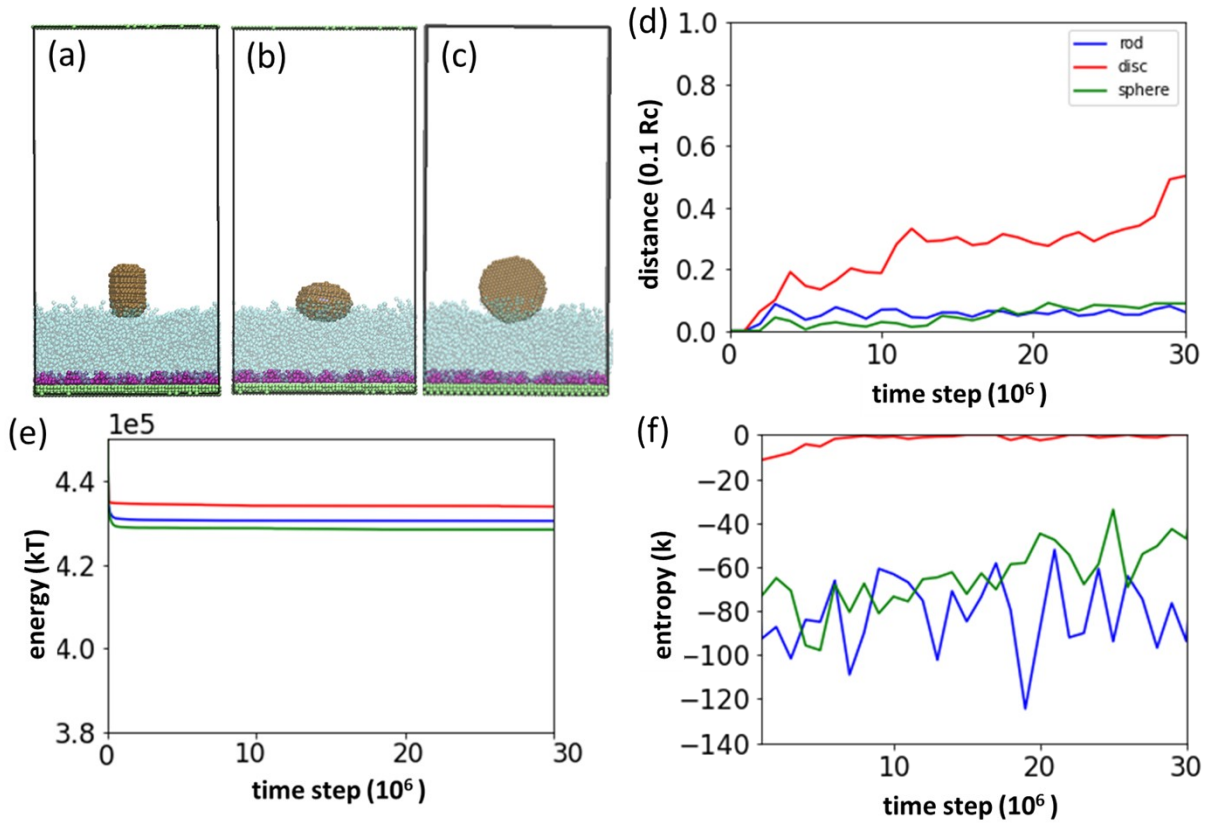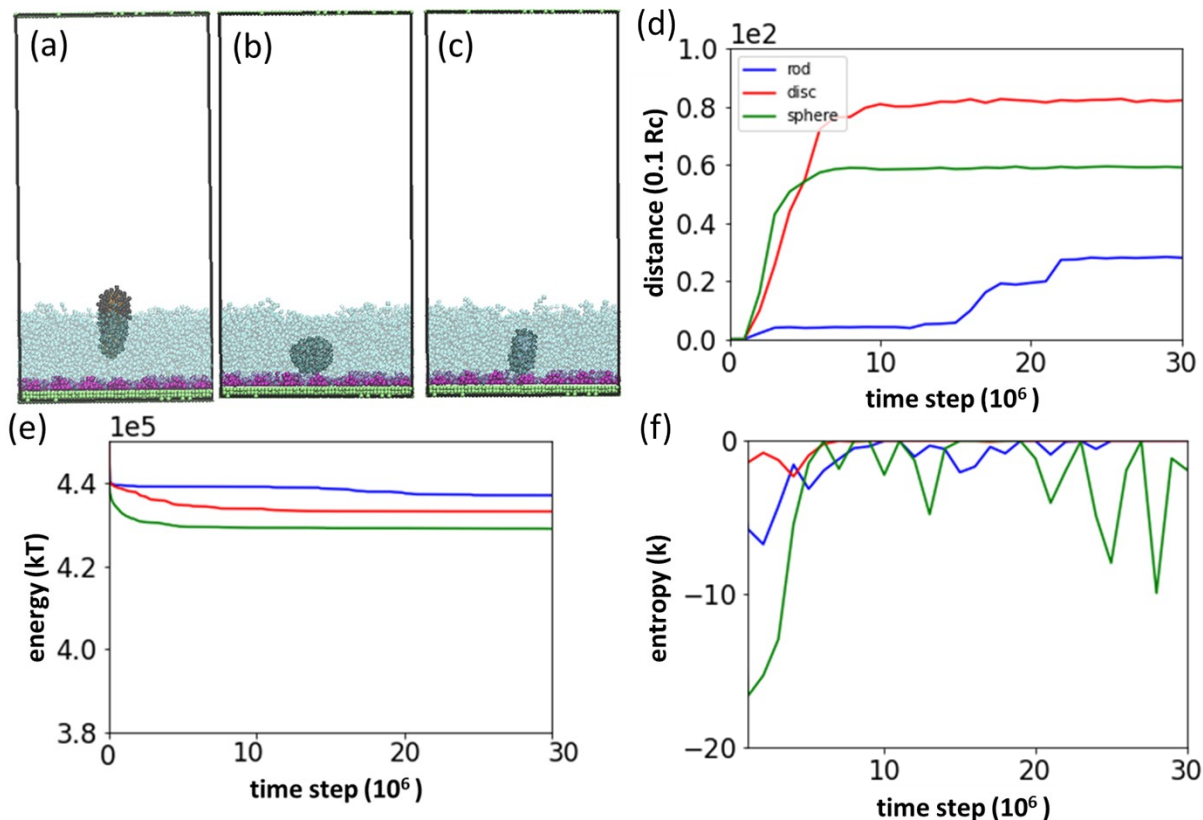


Figure S1. VMD snapshots of (a) rod, (b) sphere, and (c) disc shapes of 12rc bare NCs after $30*10^5$ time steps run. The time evolution of (d) Z_MSD, (e) potential energy, and (f) shell entropy of 12rc bare NCs with different shapes.

Figure S2 compares the penetration of 8 $R_c$ functionalized NCs with different shapes. The time evolution of Z_MSD, potential energy and shell entropy of the rod, sphere, and the disc are compared.



Figure S2. VMD snapshots of (a) rod, (b) sphere, and (c) disc shapes of 8rc functionalized NCs after $30*10^5$ time steps run. The time evolution of (d) Z_MSD, (e) potential energy, and (f) shell entropy of 8rc functionalized NCs with different shapes.

In figure S3 we compare the density profile of 12 $R_c$ functionalized NCs with different shapes at the beginning of penetration step and at the end of simulation.
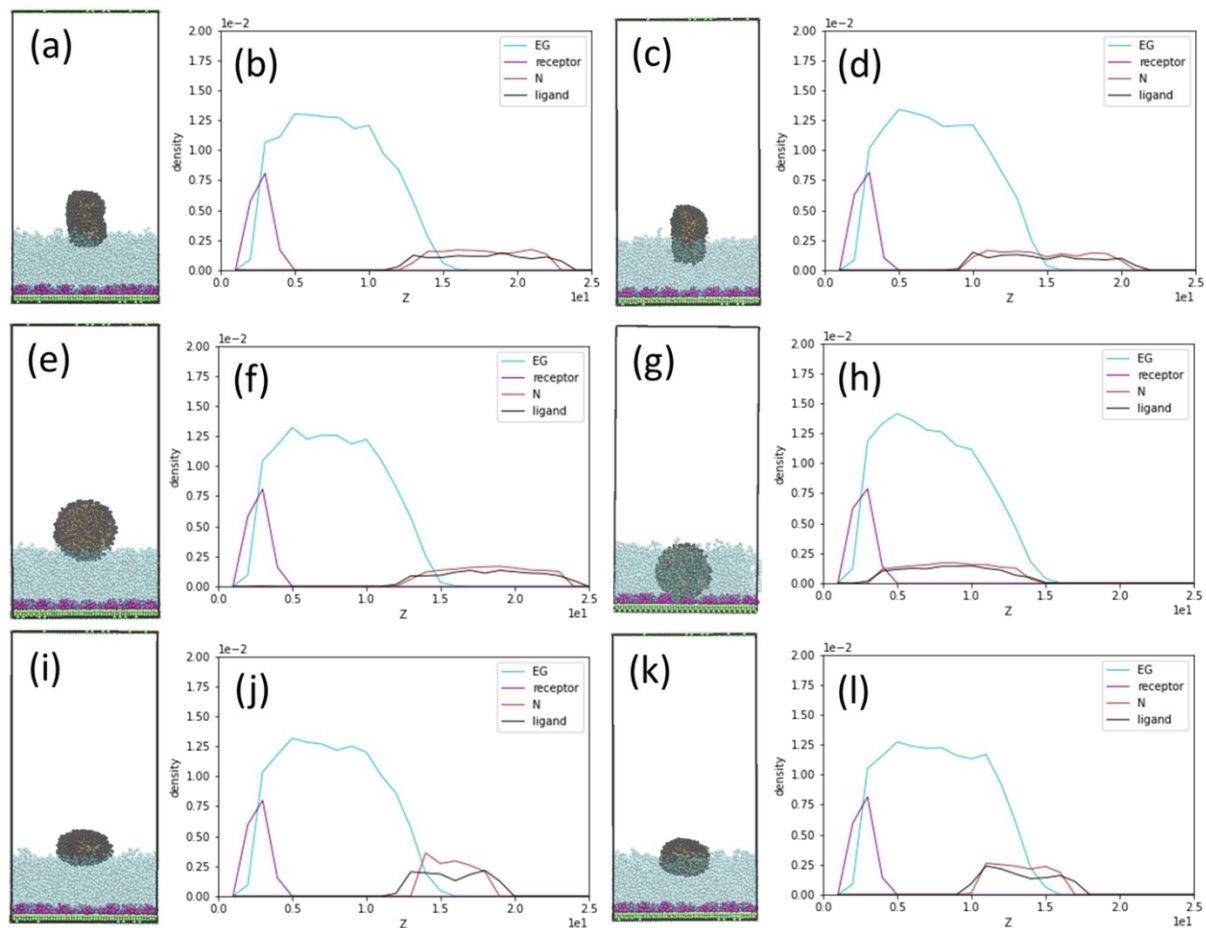
Figure S3. VMD snapshot and density profile of (a), (b), (c), and (d) rod, (e), (f), (g), and (h) disc, and (i), (j), (k), and (l) sphere shapes of 12rc functionalized NCs at 0 time step and after $30*10^5$ time steps.

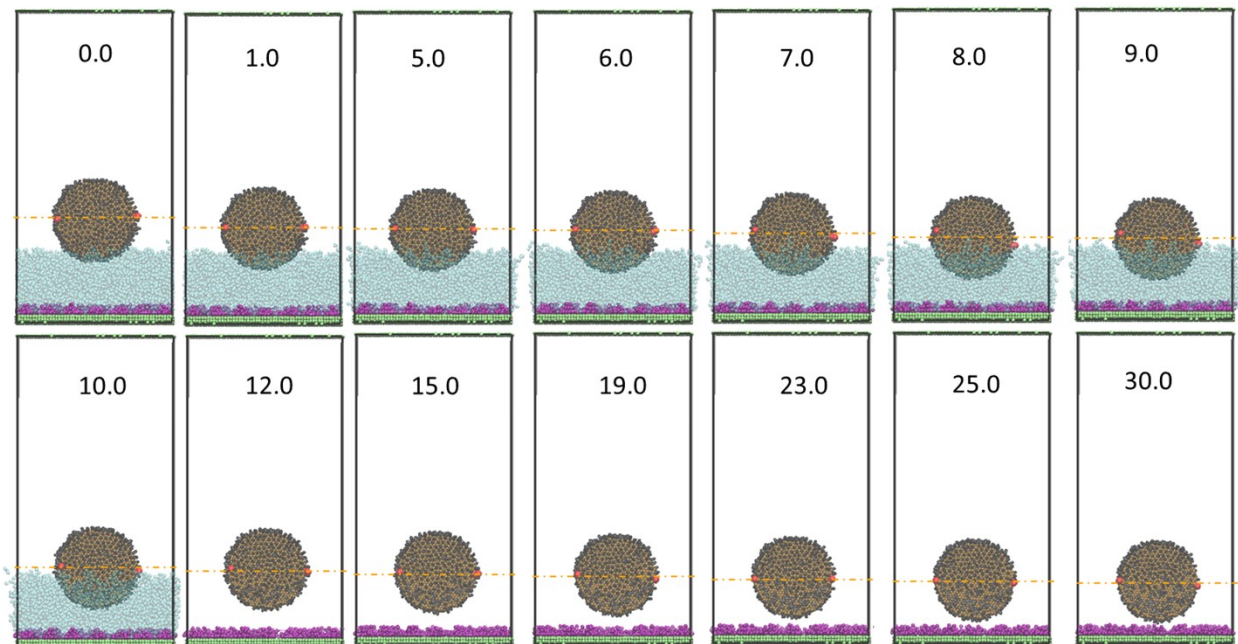Figure S4 demonstrates the time evolution of penetration of 16 $R_c$ functionalized disc into the EG layer.

Figure S4. VMD snapshots of the 16rc functionalized disc during the $30*10^5$ time steps run. The two ligands at the two opposite sides of the disc are shown in red so that the rotation of the disc versus a parallel line to the wall (orange dashed line) can be observed.

In figure S5 we explore the initial orientation effect on penetration of the 8 $R_c$ functionalized rod. The time evolution of Z_MSD, potential energy and shell entropy of parallel and perpendicular orientations are compared.

## II. Effect of initial orientation
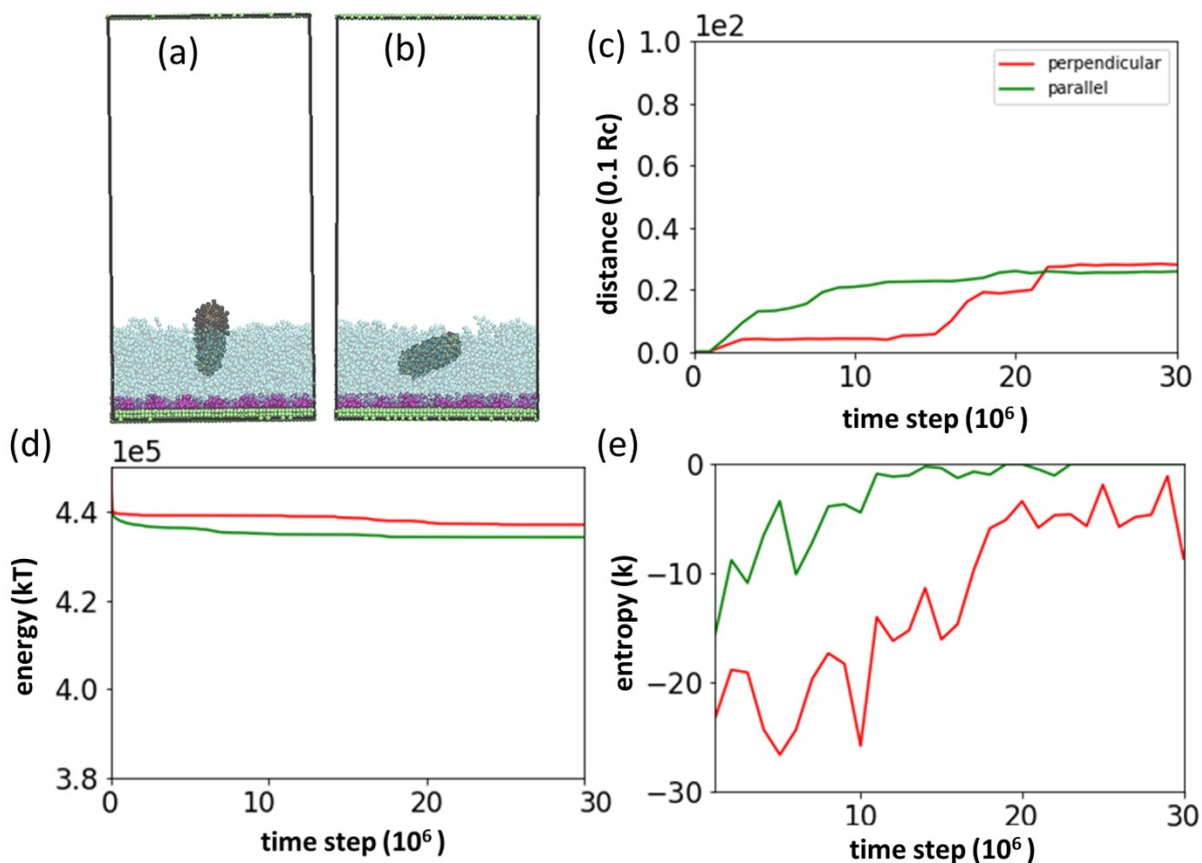


Figure S5. VMD snapshots of (a) perpendicular, and (b) parallel orientation of 8rc functionalized rod after $30*10^5$ time steps run. Time evolution of (d) Z_MSD, (d) potential energy, and (e) shell entropy of 8rc functionalized rod with different initial orientations.

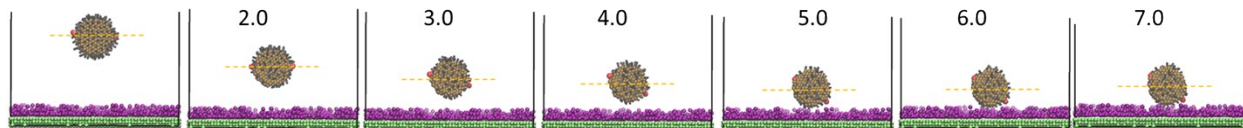In figure S6 we show the time evolution of penetration of the $8$ $R_c$ functionalized disc into the EG layer.



Figure S6. VMD snapshots of the 8rc functionalized disc during the $7*10^5$ time steps run (until the disc reaches to the receptor area). The two ligands at the two opposite sides of the disc are shown in red so that the rotation of the disc versus a parallel line to the wall (orange dashed line) can be observed.

The time evolution of penetration of the 12 $R_c$ functionalized disc into the EG layer is illustrated in figure S7. The X_MSD of disc with initial parallel and perpendicular orientation are compared in this figure.
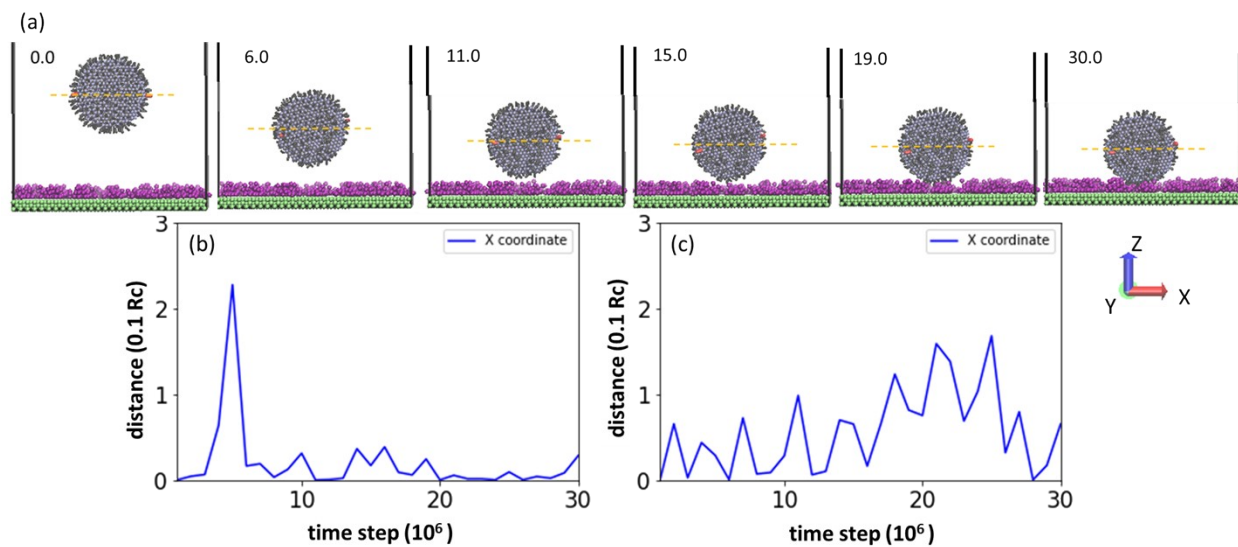


Figure S7. (a) VMD snapshots of the 12rc functionalized disc during the $30*10^5$ time steps run. The two ligands at the two opposite sides of the disc are shown in red so that the rotation of the disc versus a parallel line to the wall (orange dashed line) can be observed. (b) The X_MSD of the parallel and (c) perpendicular initial orientations

In figure S8 we show initial orientations of a disc on top of the EG layer. $\emptyset$ =90 is for parallel disc and $\emptyset$ =0 is for perpendicular disc.
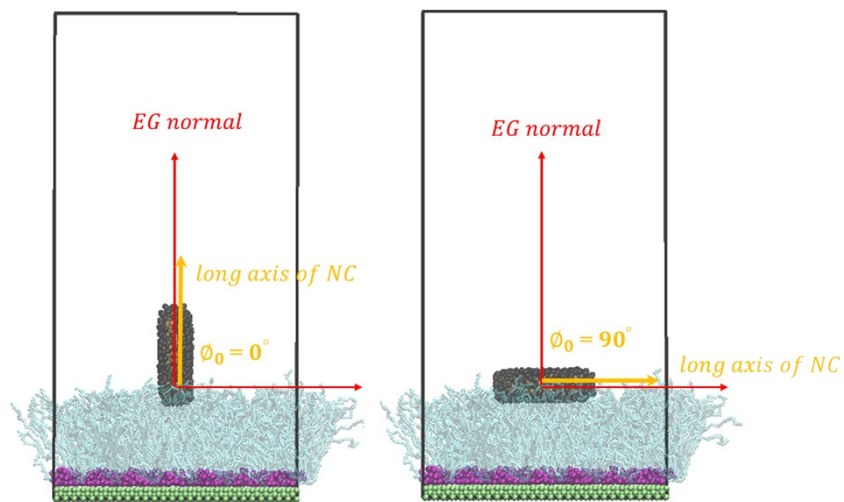


Figure S8. Schematic showing the angle $\emptyset$ between the long axis of the NC and the EG layer normal at initial step where t = 0 and $\emptyset = \emptyset_0$.
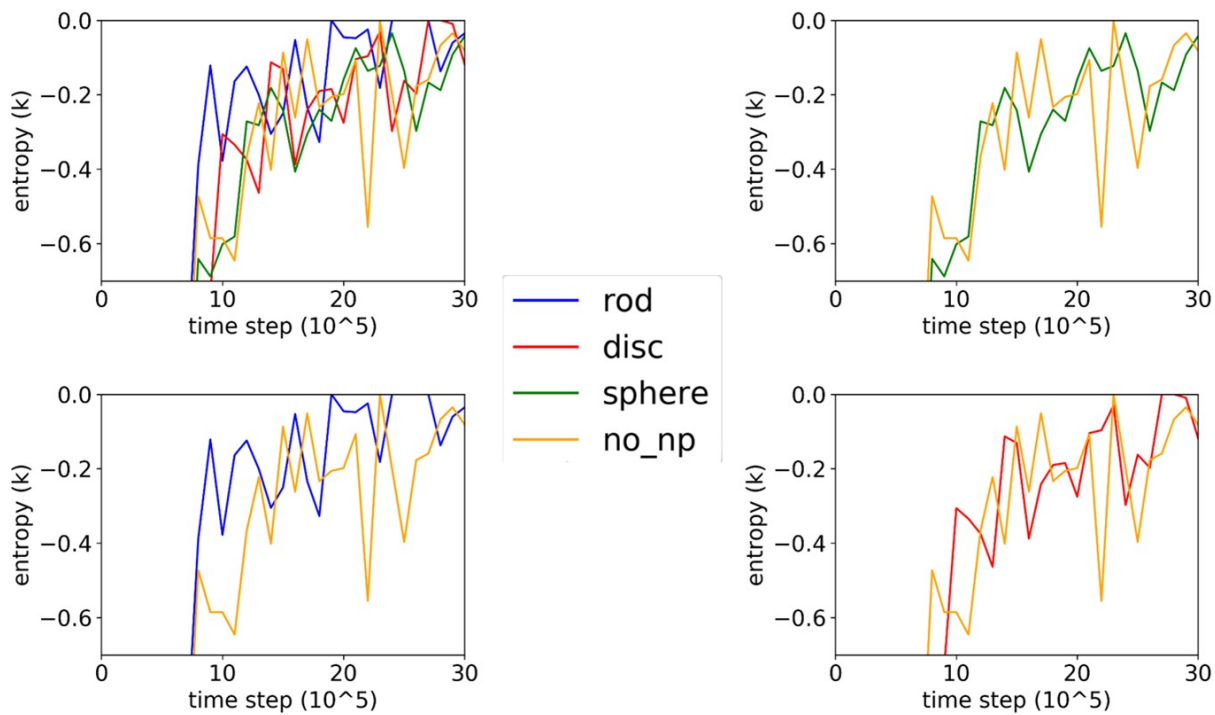
## III. EG entropies



Figure S9. Time evolution of EG entropy of 12 $R_c$ functionalized NCs with different shapes. The yellow curve is for unembedded EG chains.
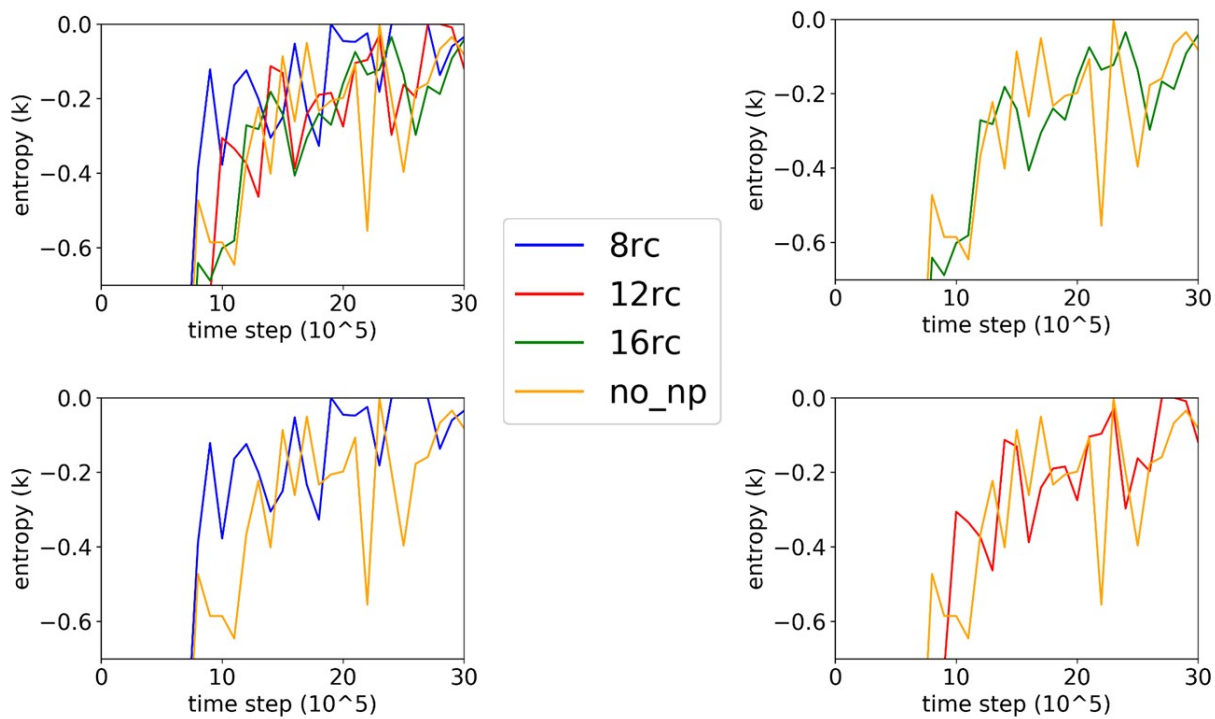
Figure S10. Time evolution of EG entropy of disc shape NCs with different sizes. The yellow curve is for unembedded EG chains.
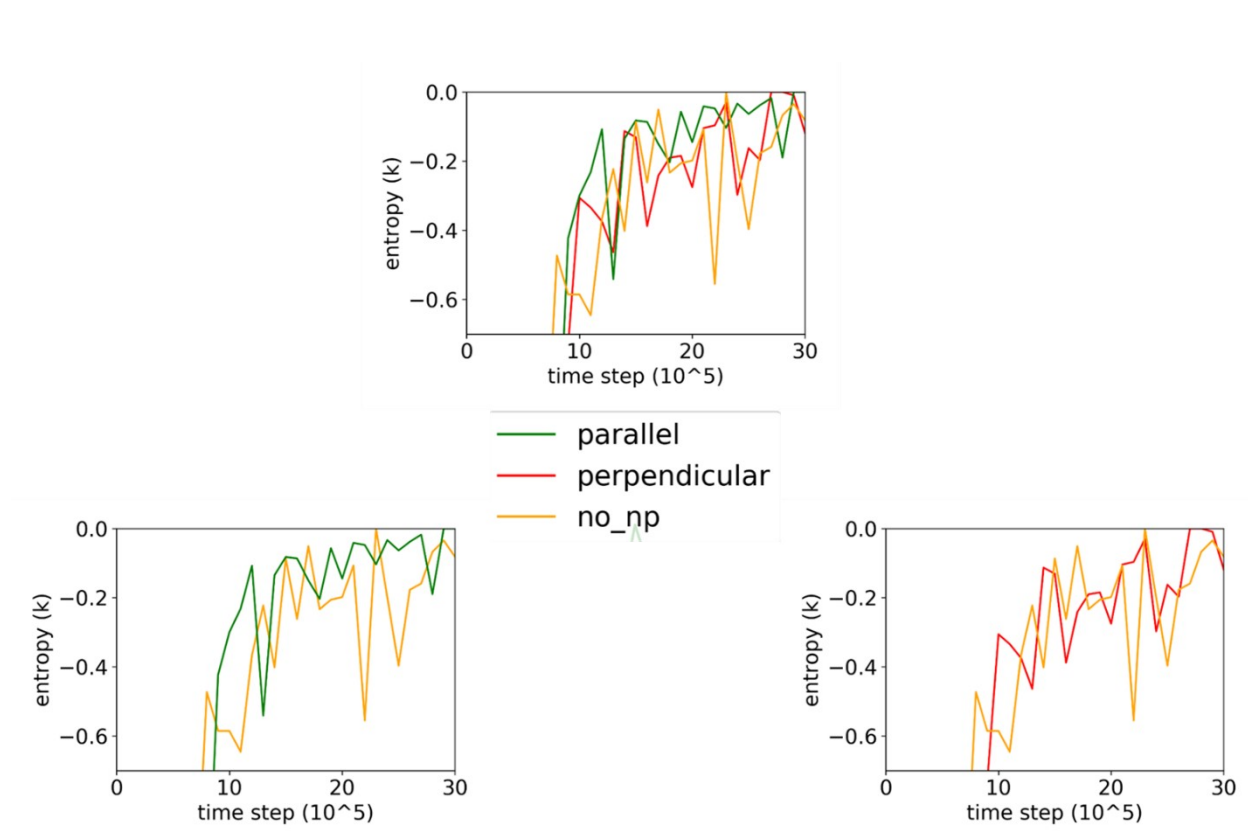
Figure S11. Time evolution of EG entropy of 12 $R_c$ disc shape NCs with different initial orientations. The yellow curve is for unembedded EG chains.
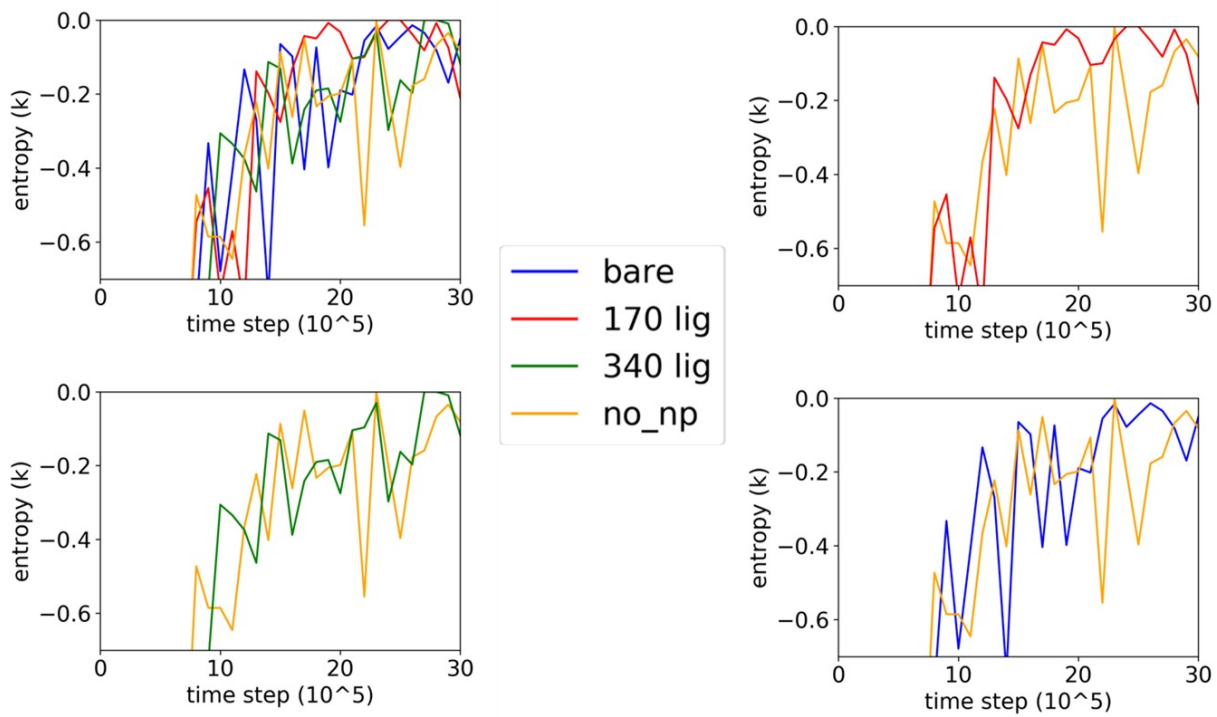
Figure S12. Time evolution of EG entropy of 12 R$_c$ disc shape NCs with different ligand densities. The yellow curve is for unembedded EG chains.
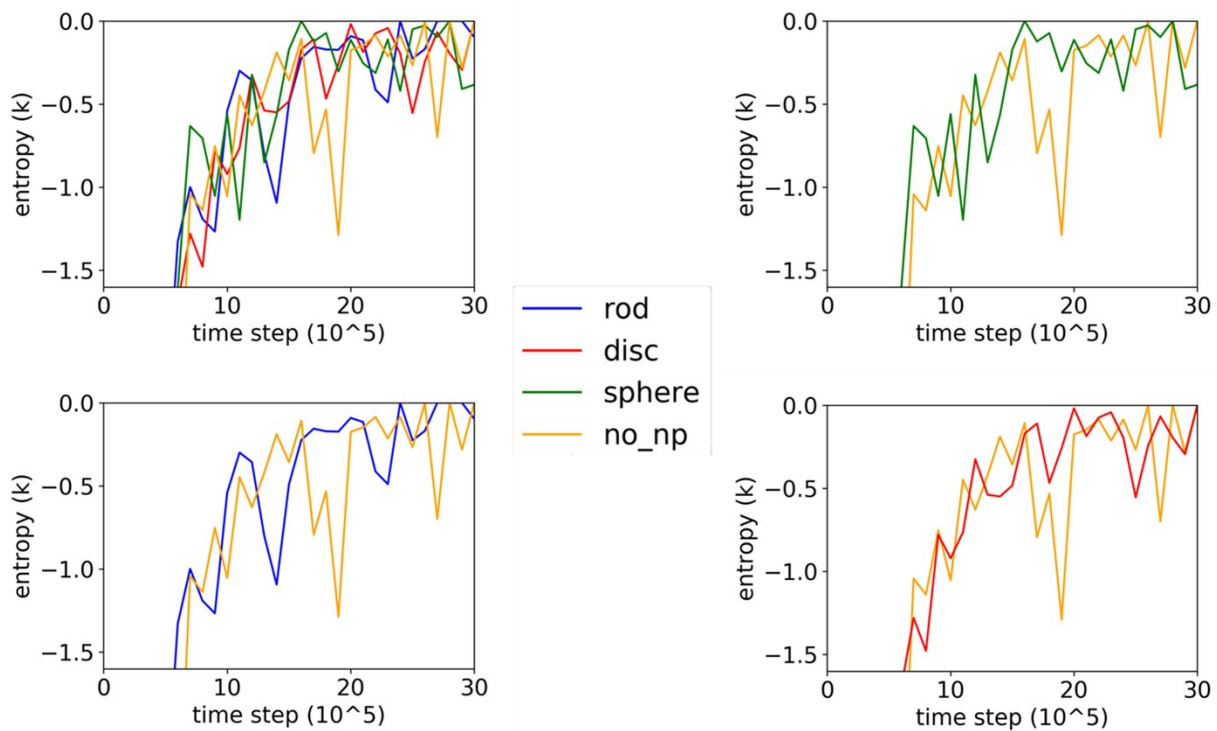
## IV. Receptor entropies



Figure S13. Time evolution of the receptor entropy of 12 $R_c$ functionalized NCs with different shapes. The yellow curve is for unembedded EG chains.
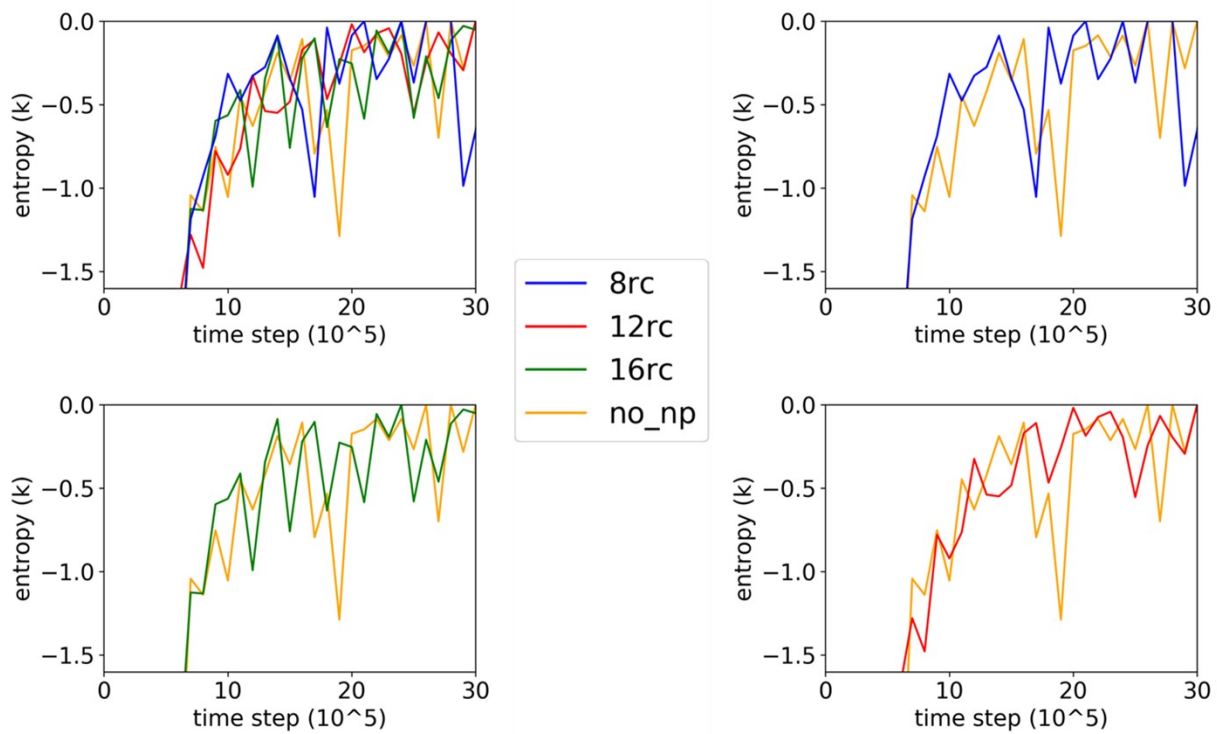
Figure S14. Time evolution of the receptor entropy of disc shape NCs with different sizes. The yellow curve is for unembedded EG chains.
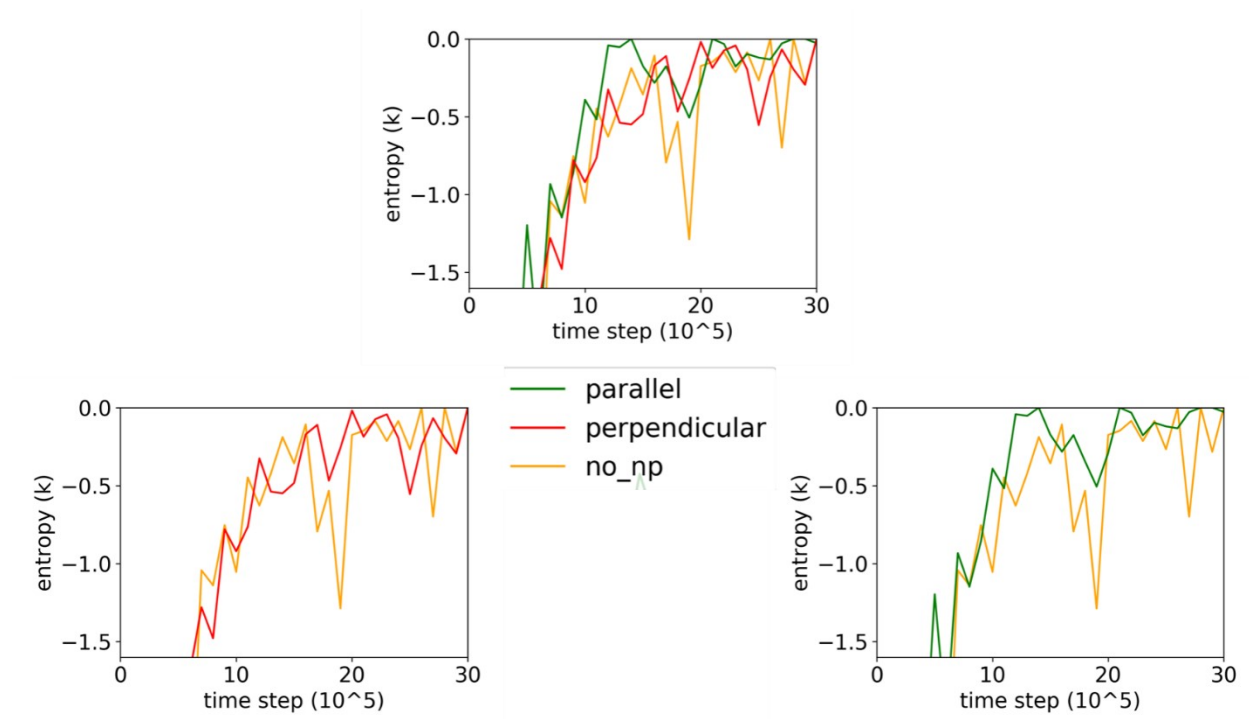
Figure S15. Time evolution of the receptor entropy of 12 $R_c$ disc shape NCs with different initial orientations. The yellow curve is for unembedded EG chains.
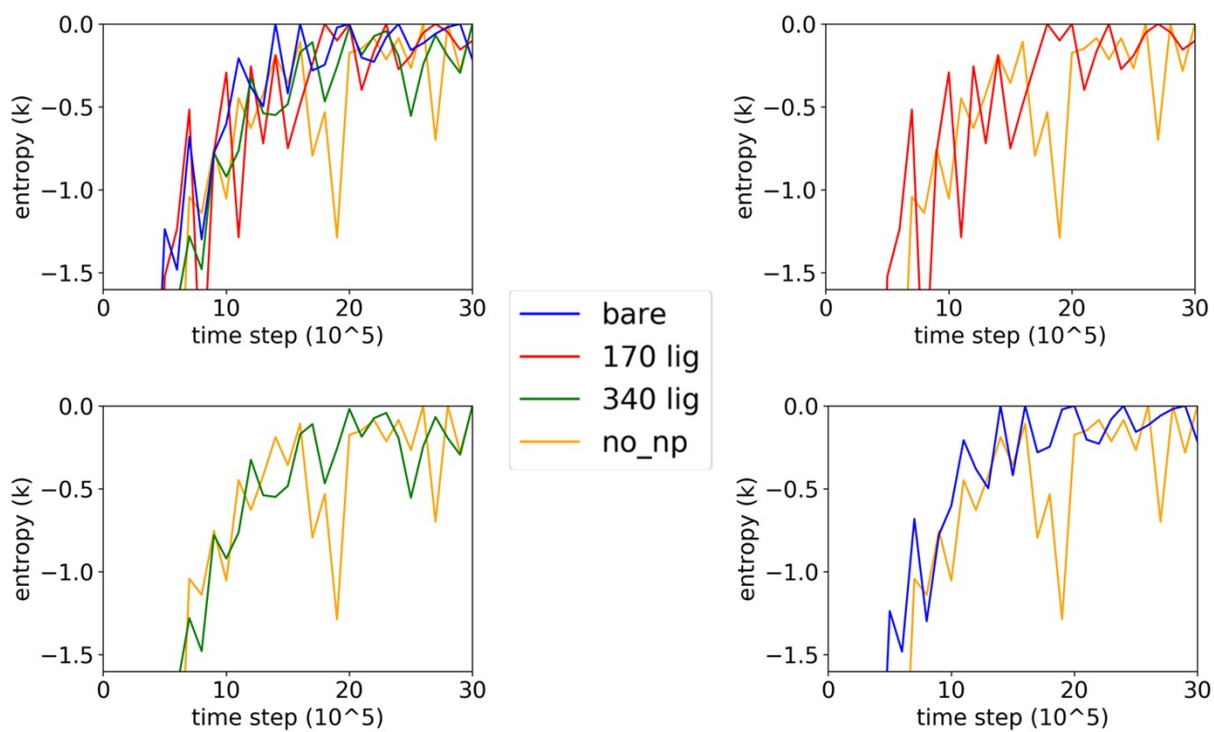
Figure S16. Time evolution of the receptor entropy of 12 $R_c$ disc shape NCs with different ligand densities. The yellow curve is for unembedded EG chains.

(1)     Koelman, J. M. V. A.; Hoogerbrugge, P. J. Dynamic Simulations of Hard-Sphere Suspensions Under Steady Shear. *Europhys. Lett. Eur. Lett* **1993**, *21* (3), 363–368.

(2)     Cheng, J.; Vishnyakov, A.; Neimark, A. V. Adhesion of Nanoparticles to Polymer Brushes Studied with the Ghost Tweezers Method. *J. Chem. Phys.* **2015**, *142* (3), 034705. https://doi.org/10.1063/1.4905894.

(3)     Groot, R. D.; Warren, P. B. Dissipative Particle Dynamics: Bridging the Gap between Atomistic and Mesoscopic Simulation. *J. Chem. Phys.* **1997**, *107* (11), 4423–4435. https://doi.org/10.1063/1.474784.

(4)     Agrawal, N. J.; Radhakrishnan, R. The Role of Glycocalyx in Nanocarrier-Cell Adhesion Investigated Using a Thermodynamic Model and Monte Carlo Simulations †. https://doi.org/10.1021/jp074514x.

(5)     Fu, B. M.; Tarbell, J. M. Mechano-Sensing and Transduction by Endothelial Surface Glycocalyx: Composition, Structure, and Function. *Wiley Interdiscip. Rev. Syst. Biol. Med.* **2013**, *5* (3), 381–390. https://doi.org/10.1002/WSBM.1211.

(6)     Liu, J.; Weller, G. E. R.; Zern, B.; Ayyaswamy, P. S.; Eckmann, D. M.; Muzykantov, V. R.; Radhakrishnan, R. Computational Model for Nanocarrier Binding to Endothelium Validated Using in Vivo, in Vitro, and Atomic Force Microscopy Experiments. *Proc. Natl. Acad. Sci. U. S. A.* **2010**, *107* (38), 16530–16535. https://doi.org/10.1073/pnas.1006611107.

(7)     Yaneva, J.; Dimitrov, D. I.; Milchev, A.; Binder, K. Nanoinclusions in Polymer Brushes with Explicit Solvent - A Molecular Dynamics Investigation. *J. Colloid Interface Sci.* **2009**, *336* (1), 51–58. https://doi.org/10.1016/J.JCIS.2009.03.062.

(8)     Wang, H.; Liu, Y. T.; Qian, H. J.; Lu, Z. Y. Dissipative Particle Dynamics Simulation Study on Complex Structure Transitions of Vesicles Formed by Comb-like Block Copolymers. *Polymer (Guildf).* **2011**, *52* (9), 2094–2101. https://doi.org/10.1016/j.polymer.2011.02.045.

(9)     Piaggi, P. M.; Parrinello, M. Entropy Based Fingerprint for Local Crystalline Order. *J. Chem. Phys.* **2017**, *147* (11). https://doi.org/10.1063/1.4998408.

(10)    Hadi, M.; Sefiddashti, N.; Edwards, B. J.; Khomami, B. A Thermodynamically Inspired Method for Quantifying Phase Transitions in Polymeric Liquids with Application to Flow-Induced Crystallization of a Polyethylene Melt. **2020**. https://doi.org/10.1021/acs.macromol.0c02144.

(11)    Gong, Y.; Ma, X.; Luo, K. H.; Xu, H.; Shuai, S. A Molecular Dynamics Study of Evaporation Mode Transition of Hydrocarbon Fuels under Supercritical Conditions. *Combust. Flame* **2022**, *246*, 112397. https://doi.org/10.1016/J.COMBUSTFLAME.2022.112397.

(12)    Amini, M.; Hasheminejad, K.; Montazeri, A. Experimentally Guided MD Simulation to Enhance the Shape Memory Behavior of Polymer-Based Nanocomposites: Towards Elaborating the Underlying Mechanism. *Compos. Part A Appl. Sci. Manuf.* **2020**, *138*, 106055. https://doi.org/10.1016/j.compositesa.2020.106055.

(13)    Williams, I.; Turci, F.; Hallett, J. E.; Crowther, P.; Cammarota, C.; Biroli, G.; Royall, C. P. Experimental Determination of Configurational Entropy in a Two-Dimensional Liquid under Random Pinning. *J. Phys. Condens. Matter* **2018**, *30* (9). https://doi.org/10.1088/1361-648X/aaa869.

(14)    Morishita, T. Time-Dependent Principal Component Analysis: A Unified Approach to High-Dimensional Data Reduction Using Adiabatic Dynamics. *J. Chem. Phys* **2021**, *155*, 134114. https://doi.org/10.1063/5.0061874.

(15)    Ghaffarizadeh, S. A.; Wang, G. J. Excess Entropy Scaling in Active-Matter Systems. *Journal of Physical Chemistry Letters*. 2022, pp 4949–4954. https://doi.org/10.1021/acs.jpclett.2c01415.